Ukrainian Journal of Physical Optics
ISSUE 4
2024

A METHOD FOR MEASURING THE ABSOLUTE SURFACE SHAPE OF LARGE APERTURE OPTICAL FLAT

XUDONG ZHANG[1], CHUNFENG XU[1], LEIHONG ZHANG[1*], SEN HAN[1*], BANGLIAN XU[1], DAWEI ZHANG[1], CHENZHE JIANG[1], ZHIXUAN ZHOU[1], QUAN SUN[2]

[1]University of Shanghai for Science and Technology, Shanghai 200093, China
[2]College of Advanced Interdisciplinary Studies, National University of Defense Technology
*Corresponding author: lhzhang@usst.edu.cn

Received: 01.04.2024

Abstract. The absolute shape measurement of large aperture optical flats usually requires a standard mirror with the same or larger aperture as the element to be measured as the reference surface for calibration. However, the large aperture standard mirror is difficult to process, and the measurement resolution is limited. To solve this problem, a method of measuring the absolute surface shape of a large aperture optical flat is proposed. The aperture optical flat is divided into several sub-apertures using the sub-aperture stitching method. The reference mirror shape is obtained by the odd and even function four-step absolute measurement method and separated to obtain the absolute surface shape of the sub-aperture. The immune algorithm is optimized and applied to the adjacent sub-aperture stitching to obtain the complete absolute surface shape. The 210 mm long flat crystal was measured, and the closed-loop self-test was designed to verify the correctness of the obtained reference mirror shape. The peak and valley value (PV) of reference mirror B is 53.64 nm, and the root mean square (RMS) value is 9.96 nm. The results of the closed-loop self-test are 58.63 nm and 10.86 nm, and the data are basically consistent with the surface shape diagram. The surface shape test results pass the closed-loop self-test. The absolute surface shape results after stitches are compared with those measured by a large aperture interferometer. The deviation of the PV value is less than λ/135 (λ=632.8 nm), and the deviation of the RMS value is less than λ/75. The measurement resolution is 11 times that measured by a large aperture interferometer, which fully proves the accuracy and high resolution of the method.

Keywords: interferometer, surface shape measurement, absolute measurement, sub-aperture stitching, immune algorithm
UDC: 535.4, 004.4
DOI: 10.3116/16091833/Ukr.J.Phys.Opt.2024.04022

1. Introduction

Large-diameter high-precision optical planar mirrors are widely used in major national optical systems for aerospace, extreme ultraviolet lithography, and laser inertial confinement fusion prototype devices [1-3], and the quality of their facet shape directly affects the quality of wave-front output from the optical system, so it is necessary to measure the facet shape of the large-diameter optical planar mirrors to ensure that it meets the technical specifications of the optical system. Optical interferometry [4] is widely used as a non-contact surface shape measurement method, which uses a standard mirror of the same or larger aperture as the element to be measured as a reference mirror to perform the measurement. Since the surface shape information measured by interferometry has the surface shape information of both the standard mirror and the optic element to be measured, it is necessary to determine the surface shape of the reference mirror and separate it to achieve absolute surface shape measurement. The three-surface mutual inspection method [5-7] is usually used for the absolute surface shape measurement of large-diameter optics. Lu

[8] conducted a comparative analysis of different three-surface mutual inspection methods and measured an optical flat crystal with an aperture of 300 mm. Zhao [9] realizes the absolute measurement of a 400 mm caliber optical flat crystal by adding dual displacement sensors based on three-sided mutual inspection method based on the measurement method of reverse co-axiality. These methods require three-sided mutual inspection with standard mirrors of the same size or larger size of the component to be measured, and the standard mirrors of large aperture have a long production cycle, difficult processing, and high transportation costs. The sub-aperture splicing method [10-12] saves costs by zoning the optical elements with a small-diameter interferometer and splicing them to obtain the relative face shape of the large-diameter optical elements. To obtain the absolute face shape, Li [13] proposed an algorithm to suppress the higher-order term error of the reference surface for sub-aperture splicing, and Li [14] separated the reference surface error by an algorithm by deriving the expression of the cumulative error of the reference mirror splicing. These methods calculate the reference surface error by algorithm, which increases the complexity during measurement.

For the large aperture planar absolute surface shape measurement, we propose a sub-aperture splicing method based on absolute measurement, which does not require a large aperture standard mirror as a reference mirror, and carries out absolute measurement by using a reference mirror with the same caliber of a small aperture interferometer, and obtains the information of the reference surface and separates it through the four-step absolute measurement of parity function[15, 16], and then reconstructs the tilt and translation of the surface shapes of the sub-aperture through the immune-optimized splicing algorithm to obtain the complete absolute surface shape under the unified same coordinate system. Through the immuno-optimized splicing algorithm, the tilt and translation of each sub-aperture face shape are reconstructed, and the splicing is unified under the same coordinate system to obtain the complete absolute face shape. While guaranteeing the measurement accuracy, it reduces the measurement cycle and cost, and obtains the absolute surface shape with a resolution several times larger than that of the three-plane mutual inspection method.

2. Large caliber face shape splicing error

In the actual measurement process of the sub-aperture method splicing technique, the interference fringe obtained from the interferometer measurement contains the reference mirror and the measured elements' face shape information. The reference mirror is not an ideal plane, so its face shape information cannot be ignored. The presence of the reference mirror's face shape information can affect the actual splicing results and reduce the accuracy of the splicing measurement. Fig. 1a shows two neighboring sub-apertures, W_j and W_{j+1}, for splicing, and the shaded part is the overlapping region of the two neighboring sub-apertures, W_j and W_{j+1}, on the measured element. Fig. 1b represents the reference surface shape W_r, where the overlapping region contains the surface shapes of the reference planes at different positions. Specifically, the sub-region W_{rj} includes the surface information of the left sub-aperture and W_r, while the sub-aperture W_{rj+1} includes the surface information of the right sub-aperture and W_r.

When measuring the plane mirror surface shape by interferometry, the position of the measured element needs to be adjusted to obtain an accurate plane mirror surface shape.

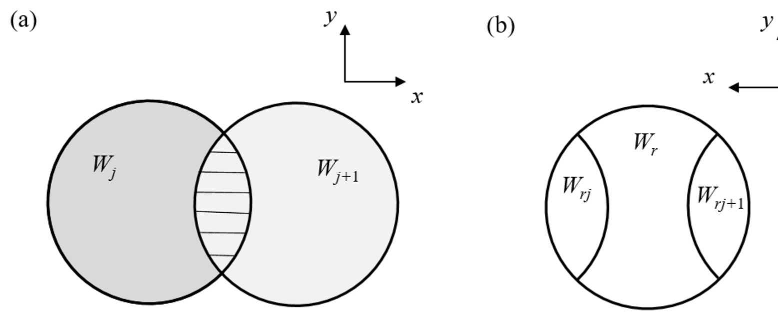

Fig. 1. Overlapping regions of adjacent sub-apertures and their corresponding influence on the shape of reference surfaces: (a) two adjacent sub-apertures; (b) reference surface shape.

Usually, the tilt angle is adjusted by a knob on the carrier stage, and the translation distance is adjusted using a guide rail under the carrier stage. The adjustments are made to reduce the number of interference fringes in the measurement range, allowing the interferometer to measure the face shape accurately. Two neighboring sub-apertures are measured with these adjustments differently. It can be seen that the tilt and translation errors of different sub-apertures need to be compensated when splicing the sub-apertures face shapes so that they are unified under the same coordinate system. Taking two neighboring sub-apertures, W_1 and W_2, as an example and establishing a Cartesian coordinate system, the relationship between W_1 and W_2 can be expressed as:

$$W_2(x,y) = W_1(x-x_0, y-y_0) + ax + by + c \,, \tag{1}$$

where x_0 is the relative displacement of neighboring sub-apertures in the *x*-direction, y_0 is the relative displacement of neighboring sub-apertures in the *y*-direction, *a* is the *x*-axis tilt slope, *b* is the y-axis tilt slope, and *c* is the *z*-axis translation. Fig. 2 illustrates the form of positional errors between neighboring sub-apertures.

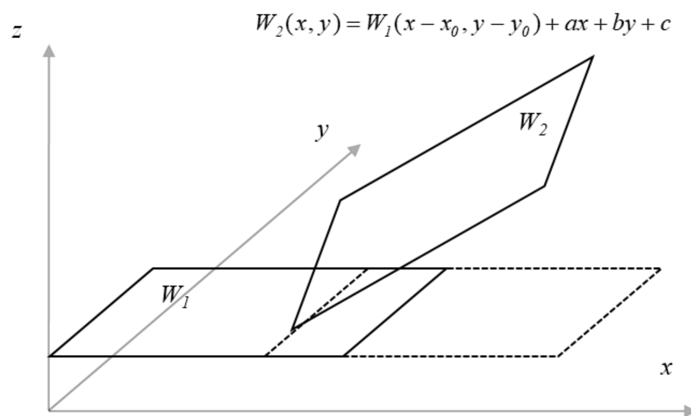

Fig. 2. Error diagram of sub-aperture.

3. Sub-aperture splicing method based on absolute measurements

3.1. Four-step absolute measurement of parity functions

In order to eliminate the influence of the face shape information of the reference mirror on the actual splicing results, the relative face shapes measured by the interferometer are separated from the absolute face shapes of the reference mirrors by the four-step absolute

measurement method of the parity function, the operation steps of which are shown in Fig. 3. The Cartesian coordinate system is established, and the face shape information of the three plane mirrors is recorded as A, B, and C. x and y indicate the direction of the plane. The plane mirrors A and B are used as the measured planes, and the plane mirror A is rotated by 90° to obtain the face shape information A_{90}. The plane mirrors B and C are used as the reference planes, and the plane mirrors B and C are flipped along the y-axis to obtain the face shape information B_x and C_x. Dividing the whole measurement process into four steps, the three plane mirrors were combined two by two, Fig. 3(b) shows plane mirror B as the reference mirror and plane mirror A as the measured mirror. According to Fig. 3(c), plane mirror A has been rotated once relative to plane mirror B, the reference mirror was replaced once in Fig. 3(d), and the measured mirror was replaced once in Fig. 3(e).

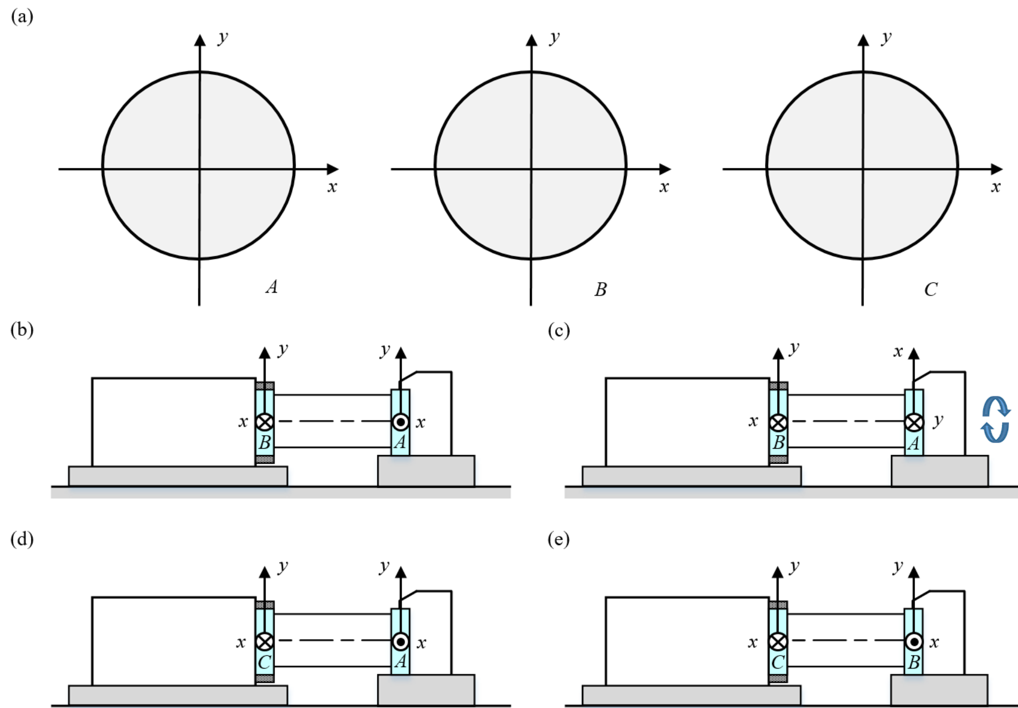

Fig. 3. Schematic diagram of the four-step absolute measurement of odd and even functions. (a) Three surface shapes in Cartesian rectangular coordinates; (b) $A+B_x$; (c) $A_{90}+B_x$; (d) $A+C_x$; (e) $B+C_x$.

Four sets of measurements M_1 , M_2 , M_3 and M_4 are obtained and their expressions are:

$$\begin{aligned} M_1 &= A+B_x, \\ M_2 &= A_{90}+B_x, \\ M_3 &= A+C_x, \\ M_4 &= B+C_x. \end{aligned} \tag{2}$$

In the Cartesian coordinate system, a two-dimensional function can be decomposed into four functional components:

$$F(x,y)=F_{ee}(x,y)+F_{oe}(x,y)+F_{eo}(x,y)+F_{oo}(x,y)\,, \tag{3}$$

where $F_{ee}(x,y)$ is the even-even function component, $F_{oe}(x,y)$ is the odd-even function component, $F_{eo}(x,y)$ is the even-odd function component, and $F_{oo}(x,y)$ is the odd-odd function

component. The facet information A, B, and C can be expressed as:

$$\begin{aligned} A &= A_{ee} + A_{oe} + A_{eo} + A_{oo}, \\ B &= B_{ee} + B_{oe} + B_{eo} + B_{oo}, \\ C &= C_{ee} + C_{oe} + C_{eo} + C_{oo}. \end{aligned} \tag{4}$$

The odd-even and even-odd function components of the plane mirrors A, B, and C are obtained from M_1, M_2, and M_3:

$$\begin{aligned} A_{oe} + A_{eo} &= \frac{1}{2}\cdot\left[\left(M_1 + (M_1)_{90}\right) - \left(M_2 + (M_2)_{90}\right)\right], \\ B_{oe} + B_{eo} &= \frac{1}{2}\cdot\left(M_1 - (M_1)_{90}\right)_x - \left(A_{oe} + A_{eo}\right)_x, \\ A_{oe} + A_{eo} &= \frac{1}{2}\cdot\left(M_3 + (M_3)_{180}\right)_x - \left(A_{oe} + A_{eo}\right)_x. \end{aligned} \tag{5}$$

In Eq. (5), $(M_i)_\theta$ represents the result of rotating M_i by an angle of θ degrees. The even-even function components of the three planes can be obtained from Eq. (5):

$$\begin{aligned} A_{ee} &= \frac{1}{4}\cdot\left[\left(m_1 + m_3 - m_4\right) + \left(m_1 + m_3 - m_4\right)_x\right], \\ B_{ee} &= \frac{1}{2}\cdot\left[\left(m_1 + m_{1(x)}\right) - 2\cdot A_{ee}\right], \\ C_{ee} &= \frac{1}{2}\cdot\left[\left(m_3 + m_{3(x)}\right) - 2\cdot A_{ee}\right]. \end{aligned} \tag{6}$$

In Eq. (6), $(\bullet)_x$ means a certain result has been flipped along the y-axis. m_1, m_2, and m_3 can be expressed as:

$$\begin{aligned} m_1 &= \frac{1}{2}\cdot\left(M_1 + M_{1(180)}\right) = A_{ee} + A_{oo} + B_{ee} + B_{oo}, \\ m_3 &= \frac{1}{2}\cdot\left(M_3 + M_{3(180)}\right) = A_{ee} + A_{oo} + C_{ee} - C_{oo}, \\ m_4 &= \frac{1}{2}\cdot\left(M_4 + M_{4(180)}\right) = B_{ee} + B_{oo} + C_{ee} - C_{oo}. \end{aligned} \tag{7}$$

The three planes' even-even function components, even-odd function components, and odd-even term function components are thus obtained. If the obtained even-even term function components are subtracted from the above equation, only a new expression containing only the odd-odd term function components will be obtained, and the new expression cannot solve the odd-odd term function components because of the linear relationship between the function components.

In the polar coordinate system, the odd-odd term function component is an odd function about, so $F_{oo}(x,y)$ can be expressed in terms of the Fourier series:

$$\begin{aligned} \left[F_{oo}(x,y)\right]_{90} &= -\sum\nolimits_{m=odd} f_{2m}\sin(2m\theta) + \sum\nolimits_{m=even} f_{2m}\sin(2m\theta), \\ F_{oo}(x,y) &= \sum f_{2m}\sin(2m\theta), \end{aligned} \tag{8}$$

where *odd* denotes odd, *even* denotes even, and f_{2m} is the coefficient of the corresponding expansion term. Since the fundamental frequency of $F_{oo}(x,y)$ is 2, Eq. (8) can be expressed as:

$$\begin{aligned} F_{oo} &= F_{oo,2\theta} = F_{oo,2odd\theta} + F_{oo,2even\theta}, \\ \left[F_{oo}\right]_{90} &= -F_{oo,2odd\theta} + F_{oo,2even\theta}. \end{aligned} \tag{9}$$

In Eq. (9) $F_{oo,2even\theta}$ an be expressed as:

$$F_{oo,2even\theta}=\sum_{m=even} f_{2m}\sin(2m\theta)=\sum_{m=1} f_{4m}\sin(4m\theta)=F_{oo,4\theta},$$
$$F_{oo,2odd\theta}=\sum_{m=odd} f_{2m}\sin(2m\theta). \tag{10}$$

$F_{oo,2odd\theta}$ can describe the odd-odd term function component for a standard plane mirror,. By rotation, it is possible to find the $2odd\theta$ term in the odd-odd term function components of the plane mirrors *A*, *B*, and *C*:

$$A_{oo,2odd\theta}=\frac{1}{2}\cdot(m_1'-m_2'),$$
$$B_{oo,2odd\theta}=\frac{1}{2}\cdot\left[(m_1')_{90}-m_2'\right], \tag{11}$$
$$C_{oo,2odd\theta}=\frac{1}{2}\cdot\left[(m_4')_{90}-m_4'+(m_1')_{90}-m_2'\right].$$

In Eq. (11) m_1', m_2', and m_4' can be expressed as:

$$m_1'=M_1-(A_{ee}+A_{oe}+A_{eo})-(B_{ee}+B_{oe}+B_{eo})_x,$$
$$m_2'=M_2-(A_{ee}+A_{oe}+A_{eo})_{90}-(B_{ee}+B_{oe}+B_{eo})_x, \tag{12}$$
$$m_4'=M_4-(B_{ee}+B_{oe}+B_{eo})-(C_{ee}+C_{oe}+C_{eo})_x.$$

The final information on the three plane mirror shapes is derived, which can be expressed as:

$$A=A_{ee}+A_{oe}+A_{eo}+A_{oo,2odd\theta},$$
$$B=B_{ee}+B_{oe}+B_{eo}+B_{oo,2odd\theta}, \tag{13}$$
$$C=C_{ee}+C_{oe}+C_{eo}+C_{oo,2odd\theta}.$$

When the sub-aperture is spliced, a plane mirror is selected as the reference mirror for measurement, and the obtained face shape result is the face shape information of the reference mirror and the measured element. After the absolute face shape information of the reference mirror is obtained, the absolute face shape of the sub-aperture is obtained by subtracting the measurement result from the reference mirror's absolute face shape, and the reference mirror and the separation of the face shape information of the reference mirror is realized.

3.2. Immuno-optimization-based face splicing method

When sub-aperture splicing is performed to compensate for the tilt and translation errors of different sub-apertures, we propose an immuno-optimization-based face splicing algorithm. The immune algorithm is an intelligent optimization algorithm artificially constructed by mimicking the biological immune mechanism and combining the gene evolution mechanism [17]. When the immune system resists antigens, the relevant cells proliferate and differentiate to produce a large number of antibodies to defend against them. Suppose the objective function and constraints are regarded as antigens, and the solution to the problem is regarded as antibodies. In that case, the solution process of the immunization algorithm is the process of the biological system resisting antigens. In order to better illustrate the working principle of the algorithm, the flow of the algorithm is shown in Fig. 4.

The key steps of the algorithm are as follows:

(1) In the immuno-optimization algorithm, the antigen is the problem to be solved, and in sub-aperture splicing, it is the tilt and translation errors for different sub-apertures: a, b and c.

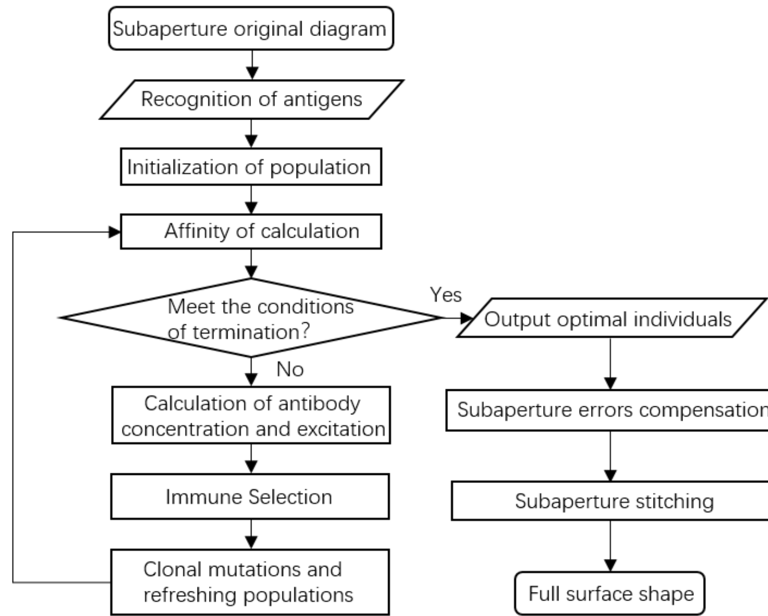

Fig. 4. Flow chart of surface stitching algorithm based on immune optimization.

(2) Initializing the population means generating N sets of initial solutions containing a, b, and c to carry as antibodies to the next operations.

(3) Evaluate the affinity of each body solution in the population. Determine whether the algorithm termination condition is satisfied: if the condition is satisfied, terminate the loop and output the optimal individual; otherwise, continue to participate in the operation to find the optimal individual. The affinity "aff" is expressed as the RMS value of the face shape residuals in the overlap region of two neighboring sub-apertures after the individual solutions in the population are brought into the compensated adjustment and localization errors.

$$\text{aff} = \sqrt{\frac{1}{t-1}\sum\sum\left(W - W_m\right)^2} \tag{14}$$

In the equation, t denotes the number of pixels in the overlapping region of two neighboring sub-apertures, W is the phase residual value of a single pixel in the overlapping region of two neighboring sub-apertures, and W_m is the average value of the phase residual value of t pixels in the overlapping region of two neighboring sub-apertures.

(4) Calculate the antibody concentration den and the incentive degree sim. The antibody concentration is an important index to evaluate the diversity of the population. A high antibody concentration means that there are a large number of individuals similar to each other in the population, and its existence is not conducive to global optimization. Antibody concentration is denoted as:

$$\text{den} = \frac{1}{N}\sum_{i=1}^{N} S_i \tag{15}$$

In Eq. (15), S_i is the solution that is more similar in distance to all other solutions in the set, taking 1 for similarity and 0 for dissimilarity. Antibody excitation is used to evaluate the quality of antibodies, which is determined by the affinity and antibody concentration together. In this

paper, the antibody with high affinity and low concentration will get a larger excitation. In Eq. (16), the m and n are normalization coefficients, indicating the weights of affinity and antibody concentration, which can be determined according to the actual situation:

$$\mathrm{sim} = m \cdot \mathrm{aff} - n \cdot \mathrm{den} \quad (16)$$

(5) Immunoselection is performed according to the antibody's excitability, and the high-quality antibody is selected for the next step. Antibodies with high excitation in the antibody group are high-quality antibodies with a higher selection value for cloning and mutation operation.

(6) Cloning and copying the high-quality antibody to obtain the number of copies, mutating the cloned copies, and replacing the antibody with a lower incentive in the population with the new cloned antibody to form a new generation of antibodies; this process is known as population refreshing, and then reevaluating the affinity. If the conditions are satisfied, then the antibodies a, b, and c with the highest affinity in the population are output and brought into Eq. (1) to unify the different sub-apertures under the same coordinate system and complete the sub-aperture splicing to obtain the full aperture face shape information.

4. Absolute surface shape verification experiment

Based on the theory in Chapter 2, we designed the corresponding absolute face shape validation experiments to measure the reference mirror face shape by the parity function four-step absolute measurement method. The improved immunity algorithm splices the absolute face shapes of each sub-aperture. The spliced absolute surface shape results are compared with the approximate absolute surface shape results directly measured by the large aperture interferometer to verify the correctness and feasibility of the method proposed in this paper.

4.1. Absolute surface shape measurement of reference surfaces

To measure the absolute surface shape of the reference plane through the parity function, the four-step absolute measurement method requires three plane mirrors with the same aperture. We use 4-inch plane standard mirrors A, B, and C for measurement (the aperture equals 101.6 mm). A 4-inch small-diameter digital Fischer phase-shift interferometer, model HOOL L6400A is used. The laser with a test wavelength of 632.8 nm is used as the light source. The four groups of measured surface profiles are shown in Fig. 5, and the measurement results are shown in Table 1.

Table 1. Results of the four-step absolute measurement method of odd and even function.

Surface shape	PV, nm	RMS, nm
M_1	69.86	13.39
M_2	56.19	11.81
M_3	91.65	19.71
M_4	69.86	13.39

PV is the peak-to-valley value, which is the distance between the highest point and the lowest point on the single plane. RMS represents the root mean square value of surface topography, which can be used to evaluate the smoothness of a surface. M_1, M_2, M_3 and M_4 are inputted into the multifunctional analysis software of the interferometer, and the relative surface shape is separated into the absolute surface shape by the software algorithm. The obtained face shapes are shown in Fig. 6. The results of the face shapes are shown in Table 2.

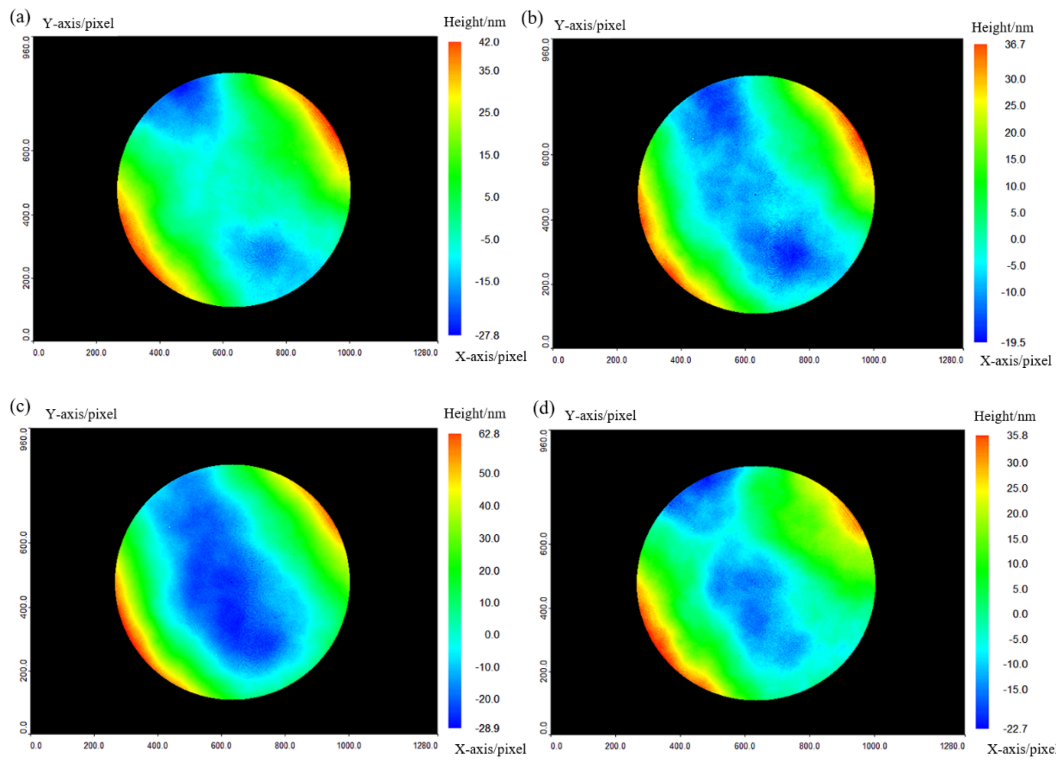

Fig. 5. Surface shapes of the four-step absolute measurement method of odd and even function. (a) M_1; (b) M_2; (c) M_3; (d) M_4.

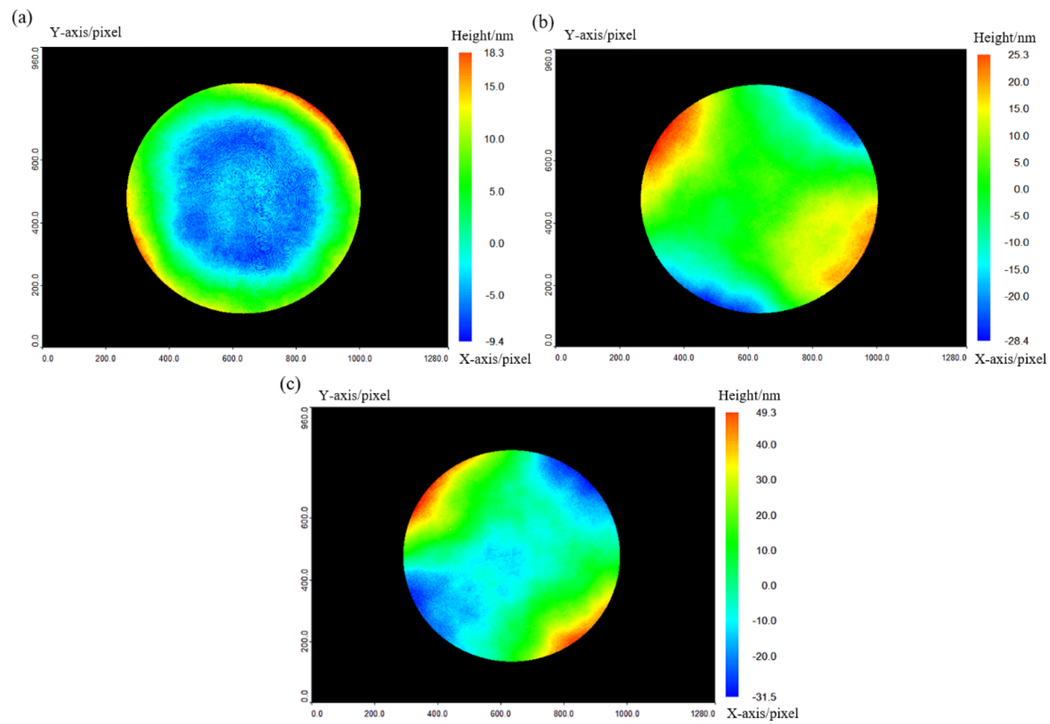

Fig. 6. Absolute surface shapes of each flat mirror. (a) absolute surface shape A; (b) absolute surface shape B; (c) absolute surface shape C.

Table 2. Absolute surface shape results of each flat mirror

Surface shape	PV, nm	RMS, nm
A	27.71	5.72
B	53.64	9.96
C	80.80	15.34

In order to verify the accuracy of the results obtained by the four-step absolute measurement method of parity function, a closed-loop self-check measurement test must be carried out on the measurement results. Closed-loop self-check means the measurement and calculation results can be matched to achieve the effect of self-check to complete the closed-loop. The closed-loop self-check measurement experiment principle is similar to the principle of interferometer measurement of surface shape. It involves subtracting the absolute surface shape result of one of the faces (which requires flipping the surface shape result along the y-axis) from the relative surface shape measurement result of the two planes, yielding the absolute surface shape data for the other face. The theoretical surface shape for the other face is based on the absolute surface shape data. We then compare this result with the results obtained by the absolute measurement method. If the surface data closely matches, the data group achieves closed-loop self-testing. The closed-loop self-checking test further proves the correctness and feasibility of the absolute measurement method by verifying the calculated and actual measurement results with each other.

In order to verify the accuracy of the absolute shape of the plane mirrors A, B, and C, a closed-loop self-check measurement test is designed for them. Using the relative measurement results of plane mirror C and plane mirror B to measure each other minus the difference of the absolute face shape data of plane mirror C after it must be flipped along the y-axis and compared with plane mirror B's absolute face shape data. If the phase distribution of the two face shape maps is relatively consistent in terms of position, and both PV and RMS values are close, it can be proved that the absolute face shape data passes the closed-loop self-checking measurement test.

B' is the absolute face shape difference between the relative measurements of plane mirror C and plane mirror B minus the y-axis flip of plane mirror C. As shown in Fig. 7a, its PV is 58.63 nm, and its RMS is 10.86 nm; Fig. 6b shows the absolute face shape B, with a PV value of 53.64 nm and an RMS value of 9.96 nm. Comparing with the data of the face shapes,

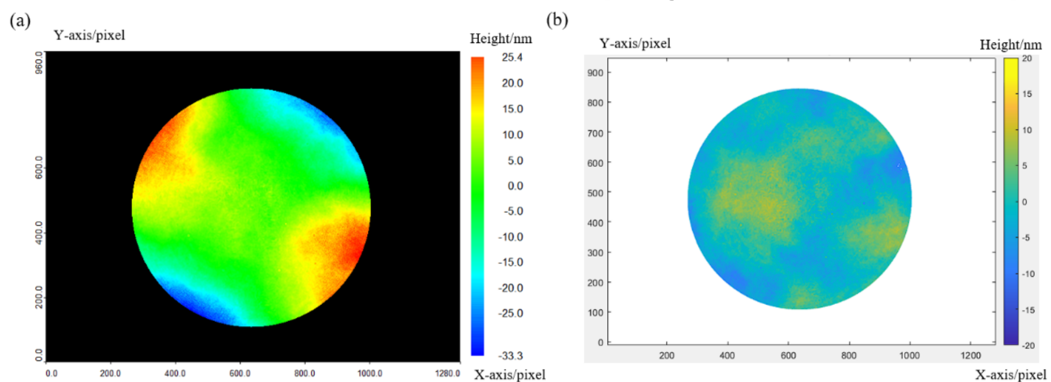

Fig. 7. The comparison of surface shapes results from a closed-loop self-test measurement: (a) B'; (b) $B' - B$.

it can be found that the two PV and RMS values are close to each other. Fig. 7b shows the residual plot of the face shape B' and the face shape B, noted as $B'-B$, with PV of 19.82 nm, RMS of 3.38 nm, and RMS can reach $\lambda/150$. By comparing the residual plots, it can be seen that the difference results in the phase distribution location of B' and the absolute face shape of the plane mirror B. The phase distribution location of the absolute face shape of the plane mirror B is more consistent. It shows that the absolute face shape data obtained by the four-step absolute measurement method of parity function can be tested by closed-loop self-check measurement, which proves that the absolute face shape data is correct and the method is feasible and effective.

4.2. Sub-aperture absolute face splice

As shown in Fig. 8a, the element under test is a 210 mm standard long flat crystal with a length of 210 mm, a width of 40 mm, and a thickness of 25 mm, and its flatness without self-gravitational deformation within the working length is -300~0 nm, and "-" indicates a depression. The system will be placed on the air-float platform, and a digital guide will be installed so that the measured components are relative to the interferometer for high-precision lateral movement while ensuring that the interferometer reference mirrors effective measurement within the aperture. Sub-aperture area planning is shown in Fig. 8b. The sub-apertures are labeled as numbers 1, 2, and 3. Label 2 is the central sub-aperture, with its center being the center point of the standard long flat crystal. To the center sub-aperture as a reference, the centers of the two adjacent sub-apertures are 65 mm apart.

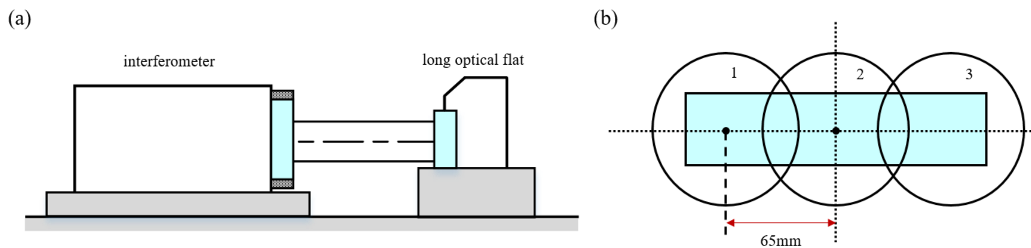

Fig. 8. Sub-aperture measurement diagram of 210 mm standard long optical flat: (a) schematic diagram of optical path system; (b) sub-aperture planning diagram.

The three sub-apertures were measured sequentially from left to right. The results of 10 sub-aperture measurements at the same location were averaged to ensure the stability of the sub-aperture information. The difference in RMS between the 10 measurements was kept within ±2 nm to ensure its repeatability. The measured sub-aperture face shape data is the relative face shape containing the reference mirror and the element under test. The measured relative sub-aperture profiles are subtracted from the absolute profile of the reference mirror to obtain the absolute sub-aperture profile that eliminates the influence of the reference mirror profile. The relative and absolute surface shapes of each sub-aperture are shown in Fig. 9, and the surface shape information is shown in Table 3.

Table 3. Surface shape results of each sub-aperture.

Surface shape	PV, nm		RMS, nm	
	relative result	absolute result	relative result	absolute result
1	112.48	114.30	14.54	17.90
2	97.55	119.57	16.42	21.06
3	104.63	116.23	15.31	19.34

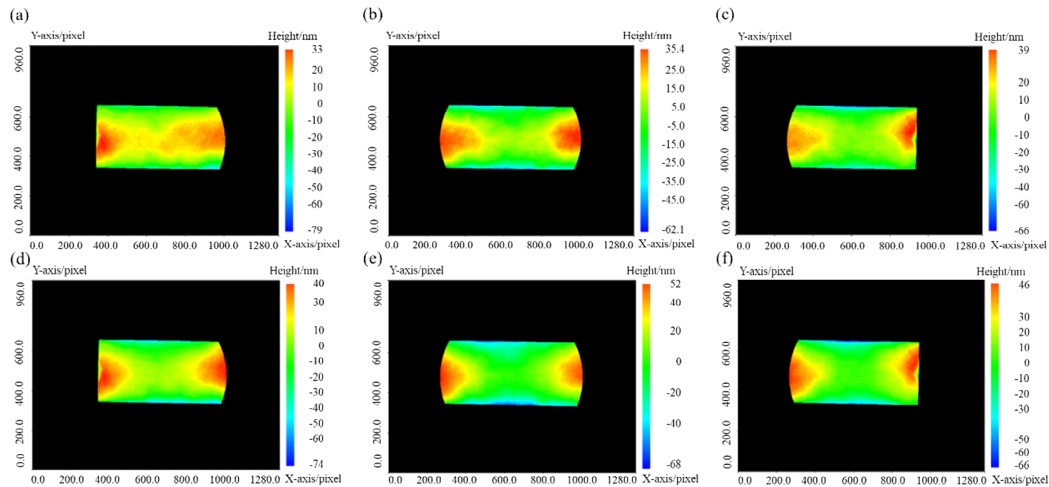

Fig. 9. Relative surface shape and absolute surface shape of each sub-aperture: (a), (b), and (c) relative surface shape; (d), (e), and (f) absolute surface shape.

The three sub-aperture absolute faceted results were derived for saving the phase values of each element in nanometers (nm) as a two-dimensional array. The central sub-aperture is taken as the reference sub-aperture and brought into the immuno-optimization splicing algorithm for calculation. The parameters to be inputted into the immuno-optimization splicing algorithm are shown in Table 4. Fig. 10 shows the affinity evolution curve when calculated by the immuno-optimization algorithm, which exhibits the trend of the evolution of the objective function in each iteration.

The x-axis is the number of iterations, the number of iterations set in this paper is 20, the axis is the value of the objective function for each iteration, in this experiment, the value of the objective function is the RMS value of the residuals of the surface shape of the overlapping region of two neighboring sub-apertures after the single solution in the population is brought into the compensation of the adjustment error and the localization error, the smaller value indicates that the two neighboring sub-apertures are more fully compensated for the splicing error, and with the multiple iterations of the value of the objective function, it finally converges to a stable value, that is, the optimal solution of the objective function. Finally, it tends to a stable value, which is, the optimal solution of the objective function is obtained. The objective function values of sub-aperture 1 and sub-aperture 3 converge rapidly in the first 7 iterations, which shows the high efficiency of the algorithm, and then converge to a stable value, that is, the optimal solution of the objective function is obtained, which shows the stability of the algorithm.

Table 4. Key parameters of the immune optimization algorithm.

Name	Parameter
Population scale N	50
The number of iterations G	20
Coefficient of affinity m	3
Coefficient of antibody concentration n	0.5
Probability of cloning P_c	40%
Probability of mutation P_m	20%
Extent of variation e	5%

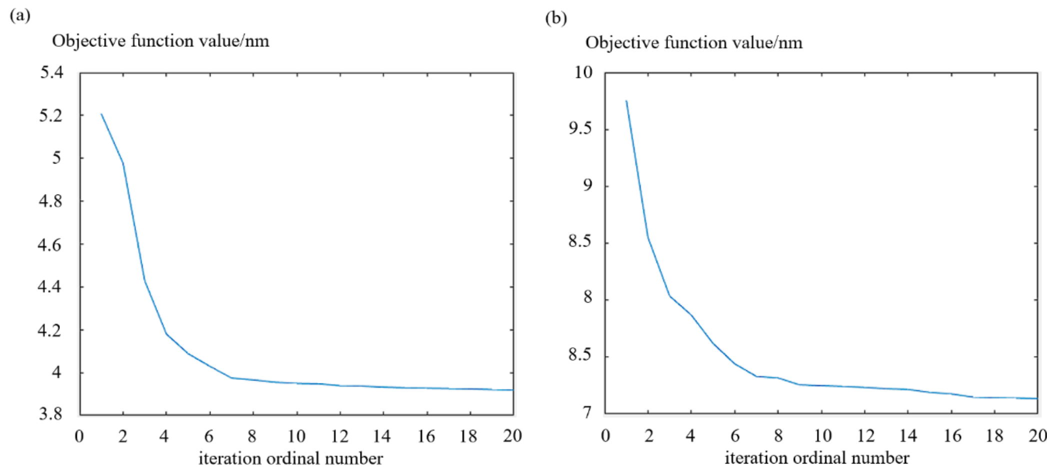

Fig. 10. Sub-aperture objective function evolution curve: (a) sub-aperture 1; (b) sub-aperture 3.

In order to verify the accuracy of the splicing results, we use a 450-mm aperture large-size interferometer to measure 210-mm long flat crystals, and the absolute face shape of the reference mirror of the large-size interferometer has been separated by the three-plane mutual inspection method. Subtract the reference mirror shape obtained from the three-sided mutual inspection method from the measurement results to obtain the absolute face shape of the full aperture of the long flat crystal in a single measurement. To ensure the stability of the measurement results, the average of the measurements taken at a single position is used for comparison. Sub-aperture splicing obtained after the full aperture absolute face shape and large aperture interferometer measurements of the absolute face shape of the 2D map and 3D map comparison is shown in Fig. 11. The phase distribution structure of the two is consistent, with high peaks on both sides of the long flat crystal and low peaks in the middle position of the long flat crystal, which can indicate that the absolute facets obtained after splicing in this paper match each other with the detection junction compared with the absolute facets obtained from the measurement of the large-diameter interferometer with a diameter of 450 mm.

The data are analyzed and the results are evaluated by the following indicators, ΔPV is the absolute value of the residual PV value of the two results in nanometers, ΔRMS is the absolute value of the residual RMS value of the two results in nanometers, ΔR is the difference of the effective pixel value of the two results in pixels, ΔPV_e is the ratio of the residual PV value of the two results in absolute value with respect to that of direct detection method, ΔRMS_e is the ratio of the residual RMS value of the two results in absolute value with respect to that of direct detection method, and ΔR_e is the ratio of the residual RMS value of the two results in absolute value with respect to that of direct detection method. ΔRMS_e is the ratio of the absolute value of the RMS residuals of the two results relative to the RMS value of the direct detection method, and ΔR_e is the ratio of the effective pixel values measured by the sub-aperture splicing method and the large aperture interferometer. Each result is shown in Table 5.

The working plane flatness standard of 210 mm standard long flat crystal is -300~0 nm, PV is the peak-valley value, which indicates the distance between the highest point and the lowest point on a single plane, the splicing PV value is 284.39 nm, and the PV value of the direct detection method is 289.08 nm, which are all in line with the working plane flatness standard of the 210 mm standard long flat crystal, among which ΔPV value is 4.69 nm, which is within λ/135, the error ratio of PV value is within 2% of ΔPV_e, which indicates the correctness and accuracy of

the splicing results. The effective pixel value of the sub-aperture splicing method is about 11 times of the effective pixel value measured by the large aperture interferometer, which indicates that the splicing method can obtain higher resolution for the same measured element, get more information about the face shape, and characterize the full aperture of the face shape more completely. Value of the deviation of each point on a single plane, reflecting the integrated deviation of the measured element's face shape and the ideal standard face shape of each point, the absolute residual value ΔRMS of the two methods, and the absolute residual value ΔPV_e is within 2%, which indicates the correct and accurate results. The absolute residual value ΔRMS of the two methods is 8.03 nm. The error ratio of RMS value ΔRMSe is 11.1%, which indicates that the results obtained by the two methods are similar. In the case of obtaining higher resolution, the RMS value of the sub-aperture splicing method is lower. The full-caliber face information obtained is smoother and more continuous, which can better express the authenticity of the detection results of the 210 mm standard long and flat crystals.

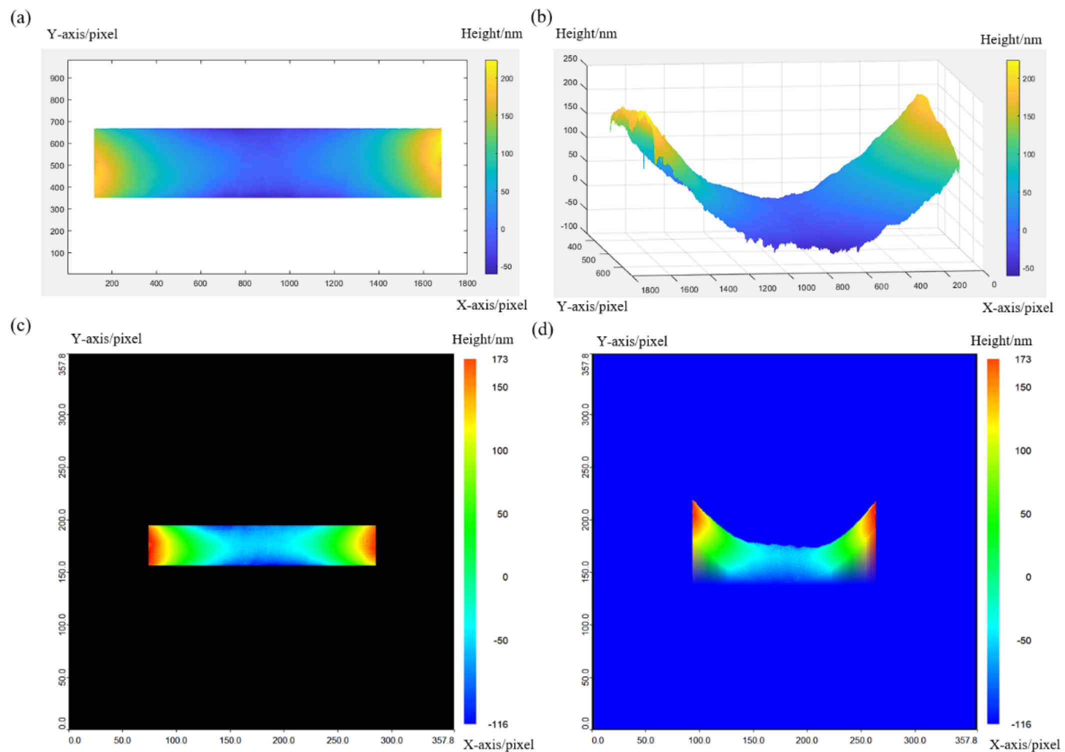

Fig. 11. Comparison of absolute surface shape between sub-aperture stitching and large aperture interferometer measurement: (a) (b) sub-aperture stitching surface shape; (c) (d) large aperture interferometer measurement surface shape.

Table 5. Comparison of results between sub-aperture stitching and large aperture interferometer measurement.

Surface shape	PV, nm	ΔPV, nm	ΔPV_e	RMS, nm	ΔRMS, nm	ΔRMS_e	Resolution, pixel	ΔR, pixel	ΔR_e
Sub-aperture stitching	284.39	4.69	1.6%	63.95	8.03	11.1%	497086	455286	11
Direct measurement	289.08			71.98			41800		

5. Conclusion

For the large-diameter plane absolute face shape measurement, we propose a sub-aperture splicing method based on absolute measurement, which reduces the number of combinations and rotations by the parity function four-step absolute measurement method, obtains the reference face information, designs the closed-loop self-check measurement test, and obtains the residual map with an RMS value of $\lambda/150$, which proves the correctness of the separated reference face shape data. In addition, this paper improves the immune algorithm to reconstruct the inclination and translation of each sub-aperture surface shape. We also completed the stitching in the same coordinate system and compared the stitching results with the measurement results of the large aperture interferometer. The experimental results prove that this method guarantees measurement accuracy and restores the high and low-frequency information lost by the large aperture interferometer during measurement, effectively expanding the surface shape resolution. It provides a cost-effective and efficient method for measuring large aperture flat absolute surface shape.

Funding

National Key R&D Program of China (Grant No.2022YFF0607701).

Acknowledgment

Authors acknowledge the support given by National Key R&D Program of China (Grant No.2022YFF0607701). In addition, authors want to appreciate the editor and anonymous reviewers for their valuable comments and suggestions to this paper.

Disclosures

The authors declare no conflicts of interest.

References

1. Zhu, J. Q., Chen, S. H., Zheng, Y. X., Huang, G., Liu, R., Tang, X., Zhang, M., Xu, Zh., Shen, L., Chen, Q., Peng, Z., Zhu, B., Zhu, Q., Tang, Y., Zhang, W., Tang, F., Liu, F., Mao, Ch., Zhu, J., Ma, W., Li, X., Yang, L., Wang, S., Yang, Y., Cai, X., Lin, Z., Fan, D., Wang, S., Gu, Y. & Deng, X. (2019). Review on development of Shenguang-Ⅱ laser facility. *Chinese Journal of Lasers*, *46*(1), 0100002.
2. Jianda, S., & Dai Yaping, X. Q. (2016). Progress on optical components for ICF laser facility. *Optics and Precision Engineering*, *24*(12), 2889-2895.
3. Jing-run, Y. U. A. N., Ping-ping, Z. H. A. N. G., Jian-bing, S. H. I., Gao-ling, Y. A. N. G., Zheng-xu, C. A. I., Bin, T. O. N. G., Hai-zheng, Z. & Yu-ping, D. O. N. G. (2022). Progress of Photoresist Materials for Extreme Ultraviolet Lithography. *Polymer Bulletin*, *35*(12), 11-25.
4. Liebl, J., Linthe, H., Sitzberger, S., & Rascher, R. (2016, June). Interferometric measurement of highly accurate flat surfaces. In *Third European Seminar on Precision Optics Manufacturing* (Vol. 10009, pp. 162-167). SPIE.
5. Schulz, G., & Schwider, J. (1967). Precise measurement of planeness. *Applied Optics*, *6*(6), 1077-1084.
6. Fritz, B. S. (1984). Absolute calibration of an optical flat. *Optical Engineering*, *23*(4), 379-383.
7. Ai, C., & Wyant, J. C. (1993). Absolute testing of flats by using even and odd functions. *Applied Optics*, *32*(25), 4698-4705.
8. Kong, L. (2020). *Research on absolute test technology of Φ 300 mm optical flat.* (publication No 000397) [Doctoral dissertation, Nanjing University of Science and Technology].
9. Zhao, Y L, Li, J F, Xu, Q. (2021). Surface Measurement Method Based on Reverse Coaxial Mode for Large Aperture Plane Optical Elements. Acta Metrologica Sinica, *42*(12), 1571-1578.
10. Kin, C. J., & Wyant, J. C. (1981). Subaperture test of a large flat or a fast aspheric surface. *Journal of the Optical Society of America (1917-1983)*, *71*, 1587..
11. Wei, H., Hu, H., Yan, F., Chen, X., Cheng, Q., Xue, D., & Zhang, X. (2018). Multi-beam array stitching method based on scanning Hartmann for imaging quality evaluation of large space telescopes. *Scientific Reports*, *8*(1), 7272.
12. Zhang, M., Tian, W., Peng, J., Sui, Y.-X., Yang, H.-J. (2013). Mechanical positioning error compensation algorithm for subaperture stitching interferometry. Journal of Optoelectronics·Laser, *24*(09): 1745-1751.

13. Li, M. Y., Cao, T. F., Yuan, X. D., Zhang, J., Liu, C., Yi, C., Chen, H., Quan, X. (2019). Effect of Reference Surface Error on Subaperture Stitching for Flat Optics. Chinese Journal of Lasers, *46*(12), 1204006.
14. Li, Y., Tang F, Lu, Y. J., Wang, X., Guo, F., Li, J., Wu, F. (2015). A Method for Reducing the Error Accumulation in Sub-Aperture Stitching Interferometer for Flat Optics. Chinese Journal of Lasers, *42*(07), 0708006.
15. Yuchen, L., Sen, H., Quanying, W., Shouhong, T., Xueyuan, L., & Quanzhao, W. (2017). Absolute test of flats based on even or odd functions. *Journal of Applied Optics*, *38*(3), 469-475.
16. Zhang, L. H., Han, S., Wu, Q. Y., Tang Sh-h., Li X-y., Wang Q-z. (2019). Absolute Test of Optical Planar by Closed Loop. Acta Metrologica Sinica, *40*(02), 208-212.
17. Gomathi, B., Suganthi, S. T., Prabhu, T. N., & Kovalenko, A. (2022). Multi-Objective Immune Algorithm for Internet of Vehicles for Data Offloading. *Intelligent Automation & Soft Computing*, *34*(3).

Xudong Zhang, Chunfeng Xu, Leihong Zhang, Sen Han, Banglian Xu, Dawei Zhang, Chenzhe Jiang, Zhixuan Zhou, Quan Sun. (2024). A Method for Measuring the Absolute Surface Shape of Large Aperture Optical Flat. *Ukrainian Journal of Physical Optics*, *25*(4), 04022 – 04037. doi: 10.3116/16091833/Ukr.J.Phys.Opt.2024.04022

Анотація. *Для вимірювання абсолютної форми поверхні оптичного дзеркала з великою апертурою зазвичай потрібне стандартне дзеркало з такою ж або більшою апертурою, що й елемент, що підлягає вимірюванню, як еталонна поверхня для калібрування. Однак, стандартне дзеркало з великою апертурою важко обробляти, а роздільна здатність вимірювання є обмежена. Для вирішення цієї проблеми запропоновано метод вимірювання абсолютної форми поверхні великоапертурної оптичної площини. Оптична площина апертури розділена на кілька підапертур методом підапертурного зшивання. Еталонну форму дзеркала одержують за допомогою чотирьохетапного методу абсолютного вимірювання непарної та парної функції та відокремлюють для отримання абсолютної форми поверхні субапертури. Імунні алгоритми оптимізовано та застосовано до сусідніх субапертурних швів, щоб отримати повну абсолютну форму поверхні. Було виміряно плоский кристал довжиною 210 мм, і було розроблено самоперевірку замкнутого циклу, щоб перевірити правильність отриманої форми еталонного дзеркала. Пікове та мінімальне значення (PV) еталонного дзеркала B становить 53,64 нм, а середньоквадратичне значення (RMS) становить 9,96 нм. Результати самоперевірки замкнутого контуру становлять 58,63 нм і 10,86 нм, і ці дані, в основному, відповідають діаграмі форми поверхні. Результати перевірки форми поверхні проходять самоперевірку замкнутого циклу. Результати абсолютної форми поверхні після зшивання порівнюються з даними, виміряними інтерферометром з великою апертурою. Відхилення значення PV менше ніж λ/135 (λ=632,8 нм), а відхилення середньоквадратичного значення менше ніж λ/75. Роздільна здатність вимірювання в 11 разів перевищує виміряну великоапертурним інтерферометром, що повністю підтверджує точність і високу роздільну здатність методу.*

Ключові слова*: інтерферометр, вимірювання форми поверхні, абсолютне вимірювання, субапертурне зшивання, імунний алгоритм*